Chemistry Central Journal

RESEARCH ARTICLE Open Access

Structural and optical characterization of metal tungstates (MWO_4; M=Ni, Ba, Bi) synthesized by a sucrose-templated method

Siti Murni M Zawawi, Rosiyah Yahya*, Aziz Hassan, H N M Ekramul Mahmud and Mohammad Noh Daud

Abstract

Background: Metal tungstates have attracted much attention due to their interesting structural and photoluminescence properties. Depending on the size of the bivalent cation present, the metal tungstates will adopt structures with different phases. In this work, three different phases of metal tungstates MWO_4 (M= Ba, Ni and Bi) were synthesized via the sucrose templated method.

Results: The powders of $BaWO_4$ (tetragonal), $NiWO_4$ (monoclinic) and Bi_2WO_6 (orthorhombic) formed after calcination temperatures of 750, 650 and 600°C for 4 h respectively are found to be crystalline and exist in their pure phase. Based on Scherrer estimation, their crystallite size are of nanosized. BET results showed $NiWO_4$ has the highest surface area. $BaWO_4$ exhibited less Raman vibrations than the $NiWO_4$ because of the increased lattice symmetry but Bi_2WO_6 showed almost the same Raman vibrations as $BaWO_4$. From the UV-vis spectra, the band gap transition of the metal tungstates are of the order of $BaWO_4$ > Bi_2WO_6 > $NiWO_4$. Broad blue-green emission peaks were detected in photoluminescence spectra and the results showed the great dependence on morphology, crystallinity and size of the metal tungstates.

Conclusion: Three different phases of metal tungstates of $BaWO_4$ (scheelite), $NiWO_4$ (wolframite) and Bi_2WO_6 (perovskite layer) in their pure phase were successfully prepared by the simple and economical sucrose-templated method. The highest surface area is exhibited by $NiWO_4$ while largest band gap is shown by $BaWO_4$. These materials showed promising optical properties.

Keywords: Metal tungstates, Sucrose, Optical

Introduction

Metal tungstates with formula MWO_4 have attracted much attention due to their interesting structural and photoluminescence properties [1-5]. These materials have found applications in scintillation counters, lasers and optical fibers [6,7]. Some of the divalent transition metal tungstates have also gained commercial interest in lasers and fluorescent lamps, while some are of special importance due to their electrical conductivity and magnetic properties. In addition, these materials also find applications as catalysts and humidity sensors [8,9].

In the MWO_4 compounds, if M^{2+} has small ionic radius < 0.77 Å (Ni = 0.69), it will belong to the wolframite-type monoclinic structure where the tungsten atom adopts an overall six-fold coordination [10]. However, if larger bivalent cations with ionic radius > 0.99 Å (Ba=1.35), they exist in the so-called scheelite-type tetragonal structure where the tungsten atom adopts tetrahedral coordination. Bismuth tungsten oxide belongs to the orthorhombic system, space group $Pca2_1$, and crystallizes in a layered crystal structure including the corner-shared WO_6. The Bi atom layers are sandwiched between WO_6 octahedral layers [11]. It is the simplest member of the Aurivillius family from $Bi_2A_{n-1}B_nO_{3n+3}$ (A=Ca, Sr, Ba, Pb, Bi, Na, K and B=Ti, Nb, Ta, Mo, W, Fe) (when n=1) of layered perovskites, which structurally comprises of alternating perovskite-like slabs of WO_6 and $[Bi_2O_2]^{2+}$ layers. Recently, many studies have been reported on the preparation and characterization of metal tungstates using various

* Correspondence: rosiyah@um.edu.my
Department of Chemistry, Faculty of Science, University of Malaya, Kuala Lumpur 50603, Malaysia

preparation methods such as Czochralski [12], precipitation [13,14], hydrothermal [11,15], solid state [16], pulsed laser deposition [17]. Meanwhile the nanostructures of metal tungstates in different crystal structures including nanorods, nanoparticles, hollow clusters and others have been prepared by chemical and physical methods. For Bi_2WO_6, its nanometer sheet shaped was obtained through hydrothermal treatment at pH=11, heated at 200°C for 24 hours and finally thermally treated at 400, 600 and 800°C for 3 hours [18]. $BaWO_4$ in the rhombic shape was prepared by a molten flux reaction using alkali metal nitrates as the reaction media [19]. Nickel tungstate ($NiWO_4$) nanoparticles were successfully synthesized at low temperatures by a molten salt method at a temperature as low as 270°C, where the mixture of $NaNO_3$ and $LiNO_3$ was used as the molten salt medium with 6:1 mass ratio of the salt to the $NiWO_4$ precursor [20]. Generally, these methods require expensive and sophisticated equipment, high temperatures with long processing times, expensive precursors and high consumption of electric energy.

Prabhakaran et al. [21] had used a cheaper and simpler method of using sucrose in order to synthesize yttria-stabilized zirconia (YSZ) nanoparticles in both acidic and basic solutions. The analyses consistently reported to have fairly uniform nanoparticles with small size, containing both tetragonal and monoclinic phases with crystallite size between 10 and 30 nm. Due to its simplicity, the sucrose-template method has great potential for manufacturing high quality ultrafine ceramic oxides economically [22] and this creates a new approach for synthesis of the other ceramic materials. In this method, the -OH and -COOH groups of the decomposed sucrose products help in binding the metal ions in the homogeneous solution, which reduces the chances of precipitation. During the decomposition process, a voluminous, organic-based, black, fluffy mass of carbonaceous material is formed which upon heating will decompose further into carbon dioxide and water and a large amount of heat is generated. The outgoing gases prevent agglomeration, and form pores and fine particles with high surface area in the final products. The aim of this paper is to synthesize the different crystal structures of $BaWO_4$, $NiWO_4$ and Bi_2WO_6 by a sucrose templated method and to characterize the materials for their structural and optical property by X-ray Diffraction (XRD), Field Emission Scanning Electron Microscopy (FESEM), Brunaer-Emmet-Teller (BET) and Raman spectroscopy while optical properties were investigated using UV-vis and photoluminescence spectroscopy.

Experimental details

Preparation of powders

The desired metal nitrates [$Ba(NO_3)_2$, $Ni(NO_3)_2 \cdot 6H_2O$, $Bi(NO_3)_2$] of 2.6135, 2.9081 and 4.8511 g were individually dissolved in distilled water before being mixed into an aqueous solution of sucrose. This is followed by addition of an equal volume of 2.4633 g of ammonium metatungstate to maintain stoichiometric ratio (1:1) with continuous stirring. Sucrose acts as a template and the ratio of sucrose to metal used was 3:1. Towards the end of the evaporation, the precursor solution (after further heating) gave rise to a fluffy black organic mass. The carbon rich mass was easily crushed to form the precursor powders. Precursor powders are denoted as MW*p* (M= Ba, Ni, and Bi). Calcination treatment was applied in the next step because of the large amount of organic compounds present in the crunchy powders. The temperatures and durations for calcinations were derived from the results of the thermogravimetric analysis whereby processes such as dehydration and other volatilizations to go to completion before proceeding to higher temperatures.

The calcination treatment applied to the samples involved heating at the rate of 10°C/min and the temperature was held constant for 4 h for each thermal change as inferred from the thermal analysis to allow completion of each of the processes. The three powdered precursors, MW*p* (M= Ba, Ni, and Bi) were subsequently calcined at 750, 650 and 600°C respectively for 4 h and the samples were denoted as MWO_4 (M= Ba, Ni, and Bi).

Characterization

The formation of oxides was monitored by X-ray diffraction (XRD) measurements using Siemen D5000 with a copper K_α radiation tube and wavelength λ of 1.54 Å, operated at 40 kV and 40 mA. The X-ray powder diffraction patterns were obtained in the range 5-60°, with increments of 0.05°. The crystalline phases were identified by using the International Centre for Diffraction Data (ICDD). The full width at half maximum (FWHM) of the diffraction peaks obtained from the refinement have been used to calculate the crystallite size. Specific surface area (S_{BET}) measurements were made with a Quantachrome AUTOSORB-1 model by nitrogen adsorption at -196°C using the BET isotherm. Samples were degassed under flowing argon at 250°C for 9 h before being adsorbed by nitrogen. The surface morphology of the samples was e analyzed using the Field Emission Scanning Electron Microscope, FESEM JSM-7500F/7500FA (JEOL) at magnification of 20,000 ×. This morphological analysis can provide information on the prevalent surface features. FESEM images allowed us to estimate the average particle size distribution of all three samples through the counting of approximately 150 particles using Image tool software. Diffuse reflectance spectra were obtained using a UV-Visible Spectrophotometer (Shimadzu). Raman spectra was collected by InVia Raman Microscope Renishaw spectrometer using

UV lens set at λ_{UV} = 325 nm and equipped with 2,400 l/nm diffraction grating. The same equipment was also used for photoluminesence (PL) analysis by using a visible lens set and equipped with 1,200 l/nm diffraction grating.

Results and discussion

XRD

XRD pattern can reveal the phase purity and crystallinity of the powder sample. Figure 1 shows sharp diffraction peaks indicating that the oxide products are well crystallized and no peaks attributable to other impurities were observed. The pattern agrees well with the JCPDS file of $NiWO_4$, $BaWO_4$ and Bi_2WO_6 (PDF card 72-0480, 72-0746 and 79-2381). The $NiWO_4$ indexed in wolframite monoclinic structure (space group: $P2/c$, with Z = 2) is characterized by alternating layers of transition-metal and tungsten atoms parallel to the (100) plane. The oxygen atoms are hexagonally closely packed and the metal ions occupy a quarter of all the octahedral sites [23]. For $BaWO_4$, the peaks from diffraction patterns are consistent with a body-center primitive tetragonal scheelite, space group $I4_1/a$ and has C_{4h}^6 point group with two formula units per primitive cell. In an ideal scheelite type of ABO_4, larger A (Ba^{2+}) cation shows eight-fold coordination and smaller B (W^{6+}) cation shows four-fold coordination. The tungstates reported have strong covalent bonds of W-O in $[WO_4]^{2-}$ molecular ionic units and weak coupling between $[WO_4]^{2-}$ anions and Ba^{2+} cations [24]. All the peaks of Bi_2WO_6 are recognized with the crystal structure of orthorhombic symmetry crystal phase with space group $Pca2_1$ and crystallized in a layered crystal structure including the corner-shared WO_6. The Bi atom layers are sandwiched between WO_6 octahedral layers [11].

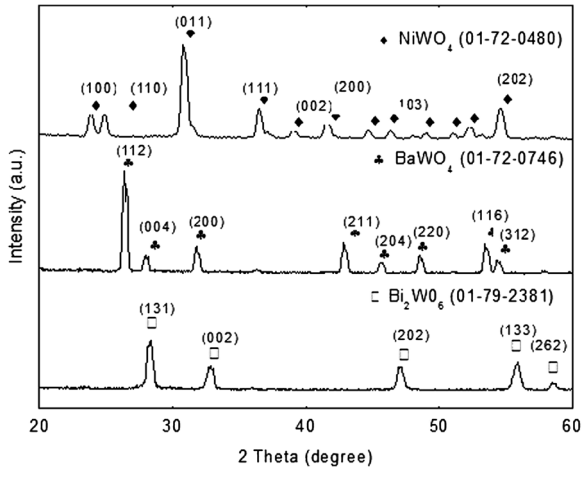

Figure 1 The XRD patterns of $NiWO_4$, $BaWO_4$ and Bi_2WO_6 samples. All samples were synthesized by sucrose template method.

Table 1 shows that crystallite sizes of all the samples calculated from Scherer's equation are in nano-size range: $NiWO_4$ at d_{100}, d_{110} and d_{011} are 19.3, 19.3 and 17.2 nm, while those of $BaWO_4$ at d_{112} and d_{004} are 18.9 and 17.4 nm. Smaller crystallite sizes of 15.5 and 14.9 nm are shown by Bi_2WO_6 at d_{131} and d_{002}, respectively. Dong Young et al. [18] have also synthesized similar compounds by commercial hydrothermal methods and obtained the crystallite size of 17-24 nm in same plane of d_{131}. $NiWO_4$ synthesized by reacting ammonium metatungstate and nickel nitrate as a function of temperature from 673 to 1073 K of 1 h reaction time has been reported by Quintana-Melgoza et al. [25] and average crystallite size as determined by Scherrer analysis obtained was from 55 to 112 nm, which is three times bigger than that reported in this work. In the case of $BaWO_4$, calculated crystallite size synthesized by room temperature the metathetic reaction method has been reported to grow twofold in crystallite size (51 nm) along d_{112} [26]. The existence of sucrose in the solution of the metal cations will form a matrix in which the metal cations are distributed through the sucrose structure. The sucrose molecule is hydrolyzed into glucose and fructose and in this way sugar recrystallization is prevented. The complex mass is obtained by complexation via gel formation and the final particles are obtained upon decomposition in the calcination process. During heating, the metal ion complex is decomposed into CO_2 and H_2O and a large amount of heat is generated. All these products are gaseous, preventing agglomeration and thus giving rise to pores and fine powders of smaller crystallite size (Table 1).

FESEM and BET

The FESEM results demonstrated that the morphology of $BaWO_4$, $NiWO_4$ and Bi_2WO_6 samples strongly depend on size of particles while BET results showed the dependency of their surface areas on pore volume and pore distribution. All three samples show different morphologies:

Table 1 Summary of metal tungstates phase formation and calculated crystallite sizes

System	X-ray phase	Crystal structure	2Θ	hkl	t (nm)
$NiWO_4$	Wolframite	Monoclinic	23.89	100	19.3
			24.85	110	19.3
			30.87	011	17.2
$BaWO_4$	Scheelite	Body cubic tetragonal	26.38	112	18.9
			27.99	004	17.4
Bi_2WO_6	Orthorhombic	Orthorhombic	28.29	131	15.5
			32.83	002	14.9

$BaWO_4$ particles (Figure 2(a)) grow in large spherical grain sizes between ~0.8-0.9 μm. Samples $NiWO_4$ and Bi_2WO_6 in Figure 2(b & c) show smaller inter-connected grain sizes of 30-90 and 20-60 nm, respectively. From Figure 3, $BaWO_4$ shows mesoporous characteristics obtained from adsorption-desorption isothermal of type IV and the H3 and the hysteresis loop observed in the range of 0.70 – 0.95 P/P_o (according to the IUPAC classification) agrees reasonably well with the small pore volume (0.05 cm^3g^{-1}) and low surface area (2.30 m^2g^{-1}), as shown in Table 2. Both samples of $NiWO_4$ and Bi_2WO_6 show adsorption-desorption isotherms of a macroporous characteristic (type III) with absence of any hysteresis loop.

Even though the $NiWO_4$ sample has larger crystallite size (according XRD), its surface area is fivefold larger (20.06 m^2g^{-1}) than Bi_2WO_6 (3.58 m^2g^{-1}). This phenomenon is attributed to the higher pore distribution (Table 2) and less agglomeration of $NiWO_4$ itself (Figure 2 (b)). This finding shows that the prepared $NiWO_4$ sample using sucrose solution evaporation has higher BET surface area compared to $NiWO_4$ synthesized by combustion method (< 11 m^2g^{-1}) even though a spherical-like morphology was obtained in both cases [27]. Bi_2WO_6 synthesized by using co-precipitation method also resulted in similar spherical particles (after calcinations at 600, 700 and 800°C) as reported by Alfaro and de la Cruz [28], but

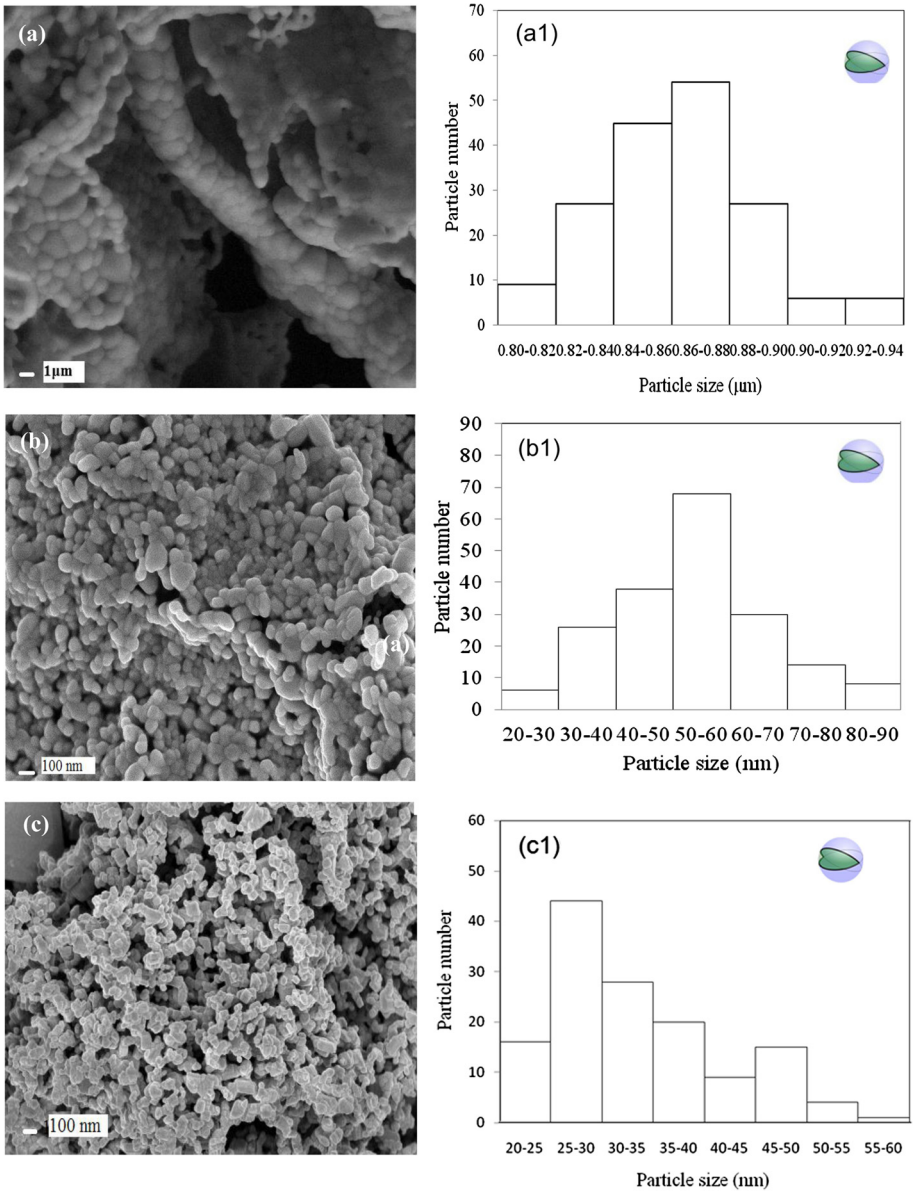

Figure 2 FESEM micrographs the metal tungstates and the calculated particle size distributions. $BaWO_4$ (**a**) (a1), $NiWO_4$ (**b**) (b1), Bi_2WO_6 (**c**) (c1).

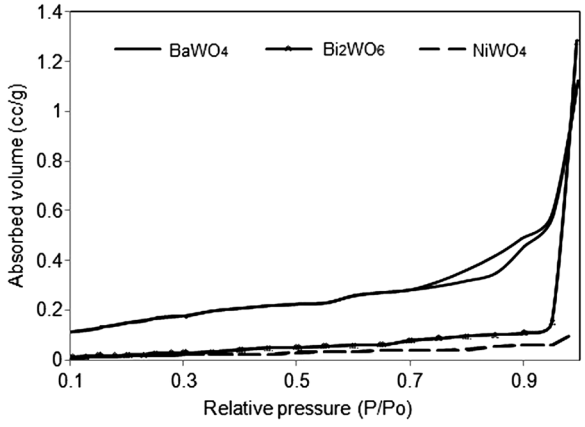

Figure 3 N_2 adsorption isotherms of $BaWO_4$, Bi_2WO_6 and $NiWO_4$ samples.

the size of particles were in microns; sizes (~1-2 μm) and BET values obtained were 0.3- 1.5 m^2g^{-1}, which was 10 times lower than the findings in this work shown in Table 2.

FESEM images can also allow the estimation of the average particle size distribution of samples by counting approximately 150 particles using an Image tool software. The particles are assumed spherical-like (Figure 2 (a1-c1)). Figure 2(a1) shows the average particle size distribution (diameter) in the range from 0.80-0.94 μm for $BaWO_4$. The figure shows that 59% of the particles with a spherical-like morphology presented an average area of 0.84-0.88 μm. Figure 2(b1) shows the average particle area distribution of Bi_2WO_6 is 20-55 nm and that 62% of the particles presented an average area of 25-35 nm, smaller than $BaWO_4$ (in micron range). As for $NiWO_4$ (Figure 2c1) with the plate-like morphology the average particle area distribution is 30-90 nm, which is in close relationship with the above grain size (FESEM image). These results show that the sucrose-templated method is able to influence the growth process into nano-range for samples $NiWO_4$ and Bi_2WO_6, except for sample $BaWO_4$ which is in micron size. However, the particle size distribution of $BaWO_4$ synthesized using a sucrose-templated method shows smaller dimension (0.84-0.88 μm) compared to $BaWO_4$ synthesized by co-precipitation followed by domestic microwave-hydrothermal at 413 K for different times which resulted in a large self-assembled microcrystal of height (0.30–11.85 μm) and width (0.25–2.30 μm) [29].

Table 2 Summary of metal tungstates specific surface area, pore volume and pore size distribution

Sample	S_{BET} (m^2g^{-1})	Pore volume (cm^3/g)	Pore size distribution, (nm)
Bi_2WO_6	3.58	0.62	1.54
$NiWO_4$	20.06	0.54	2.46
$BaWO_4$	2.30	0.05	1.92

Raman spectra

The structural order at short-range for the three different phases of $NiWO_4$, $BaWO_4$ and Bi_2WO_6 nanoparticles was determined by Raman active phonon modes (Figure 4). Hardcastle et al. [30], using the diatomic approximation method, concluded that for an ideal WO_4 unit, the shortest W-O bond should correspond to a Raman fingerprint located at 874 cm^{-1} (νs (W=O)), with a standard deviation of approximately 55 cm^{-1}.

Considering the Raman active modes of scheelite-type AWO_4 compounds, there are two types of vibration modes, belonging to the internal and external vibrations. The first corresponds to the normal motion of atoms inside the $[WO_4]^{2-}$ tetrahedrons, and the second involves the vibration WO_4 tetrahedrons against the divalent A atoms. Group theory calculation predicts 26 vibration modes for the tetragonal scheelite ($BaWO_4$) primitives' cell at wavevector k=0, which can be represented in (1) [31]:

$$\Gamma = 3A_g + 5A_u + 5B_g + 3B_u + 5E_g + 5E_u \quad (1)$$

where all 13 vibrations A_g, B_g and E_g are Raman-active. As shown in Figure 4, the tetragonal $BaWO_4$ has two strong vibrations at 924 and 330 cm^{-1} and four weak vibrations at 829, 797, 716 and 272 cm^{-1}. It is predicted to have less Raman vibrations when compared to monoclinic $NiWO_4$ because of the increased lattice symmetry. The two strong vibrations of 924 and 330 cm^{-1} and weak mode at 797 cm^{-1} can be assigned to the W-O stretching vibration of WO_4 tetrahedra. The medium mode at 272 cm^{-1} is derived from symmetric stretching vibration of the BaO_6 octahedra. All these modes are characteristic of the tetragonal scheelite structure as reported previously [32-36]. However, in our samples, the vibrations were slightly shifted and some vibration modes were not detected. These observations can be attributed to some differences in their geometries, particle sizes and nature of the products.

Comparatively, Raman vibrations for monoclinic wolframite structure would be expected to give six internal stretching modes caused by each of the six W-O bonds in the WO_6 octahedrons and from group theoretical analysis of the monoclinic ($NiWO_4$) yields 36 lattice modes [15]:

$$\Gamma = 8A_g + 10B_g + 8A_u + 8B_u \quad (2)$$

Here, 18 even (g) vibrations are Raman-active modes. As for monoclinic $NiWO_4$, the corresponding spectrum in Figure 4 shows only three strong vibrations at 891,

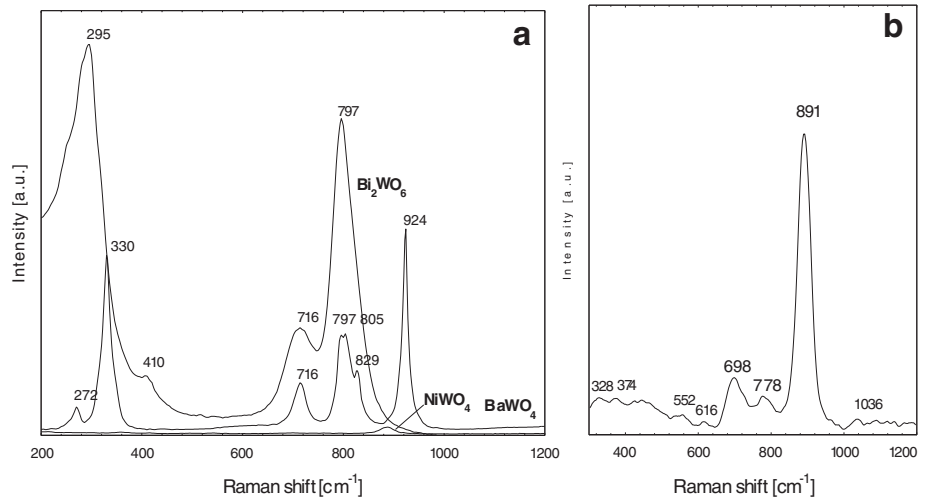

Figure 4 Raman spectra for the metal tungstates. (**a**) $NiWO_4$, $BaWO_4$ and Bi2WO (**b**) enlarged spectra for $NiWO_4$.

778 and 698 cm^{-1} and five weak vibrations at 328, 374, 552, 616 and 1036 cm^{-1} corresponding to the normal W-O vibration of the WO_6 octahedra. Unlike the ideal WO_4 structure (scheelite) where four normal vibrational modes of the tetrahedral structure are Raman active, WO_6 structure has six normal modes of vibration of which only three are Raman active. The isolated WO_6 wolframite structure found in the bulk crystalline $NiWO_4$ has 891 cm^{-1} which is associated with the WO_6 symmetric stretching vibration and this agrees well with the results reported by Ross-Medgaarden and Wachs [14].

The factor group analysis predicts that there should be 105 optical modes for $Pca2_1$ structure of Bi_2WO_6 distributed among $26A_1 + 27A_2 + 26B_1 + 26B_2$ irreducible representations. The A_1, B_1 and B_2 modes are both Raman and IR active whereas the A_2 modes are only Raman active. Bi_2WO_6 shows two strong peaks at 797 and 295 cm^{-1} and weak peaks at 410 and 716 cm^{-1}. The strongest peak at 797 cm^{-1} can be assigned to the symmetric and asymmetric stretching modes of the WO_6 octahedra involved in the motions of the apical oxygen atoms perpendicular to the layer [30]. The weak Raman peak at 716 cm^{-1}, is due to asymmetric stretching mode of the WO_6 octahedra, involving mainly vibrations of the equatorial oxygen atoms within layers. The peak at 295 cm^{-1} region originates from the bending mode of the bismuth-oxygen polyhedral.

Diffuse reflectance UV-visible spectroscopy

Figure 5 shows the optical absorption spectra of $BaWO_4$, $NiWO_4$ and Bi_2WO_6 nanoparticles with an absorption edge in 200–900 nm region. All samples have excellent optical transmission spectra as the maximum absorption edges appeared in the ultraviolet region: 223.0 nm for $BaWO_4$, 320.6 nm for Bi_2WO_6 and 299.0 nm for $NiWO_4$. The excitation from O_{2p} to Wt_{2g} in the (WO_4^{2-}) group absorbs ultraviolet irradiation in MWO_4. In the excited state of the (WO_4^{2-}) groups, the hole (on the oxygen) and the electron (on the tungsten) remain together as an exciton because of their strong interactions. Further absorption peaks in the visible region are exhibited by $NiWO_4$ which could be due to a charge transfer transition in which an oxygen $2p$ electron goes into one of the empty tungsten $5d$ orbital.

A unique feature of UV-vis for the isolated WO_4 reference compounds is that they only possess a single ligand to metal charge transfer (LMCT) band in the general region of 218-274 nm, with many of the band maxima occurring at 220-250 nm. The exact location of this band maximum depends on the extent of distortion of the isolated WO_4 structure [14]. Optical absorbances of samples $BaWO_4$ and Bi_2WO_6 show only one absorption band, while $NiWO_4$ shows four absorption bands. Worth noting to report that the absorption peak of $BaWO_4$ from this work was found close to what has been reported [19].

For the $NiWO_4$ sample, 100 nm shift to a lower wavelength was observed as compared to the same material synthesized by the molten salt method [20]. Four bands observed from the $NiWO_4$ sample at both UV and visible range (Figure 5(b)) are due to the oxidation state of the cations [37]. Cimino et al. [38] had reported that absorption bands at 1.21, 1.65-1.74, 2.00-2.11, 2.83-2.88 and 3.35 eV from $Ni^{2+}O_6$ are due to the transition from $^3A_{2g}$ to the excited states $^3T_{2g}$, ^1E_g, $^3T_{1g}$, $^1T_{2g}$, and $^3T_{1g}$, respectively. Similar data were also obtained by Lenglet et al. [39] who reported the same bands at about 1.08-1.13, 1.72-1.75, 1.77-1.95, 2.71-2.79 and 2.97-3.00 eV. In the present work, four absorbance bands at 299 nm

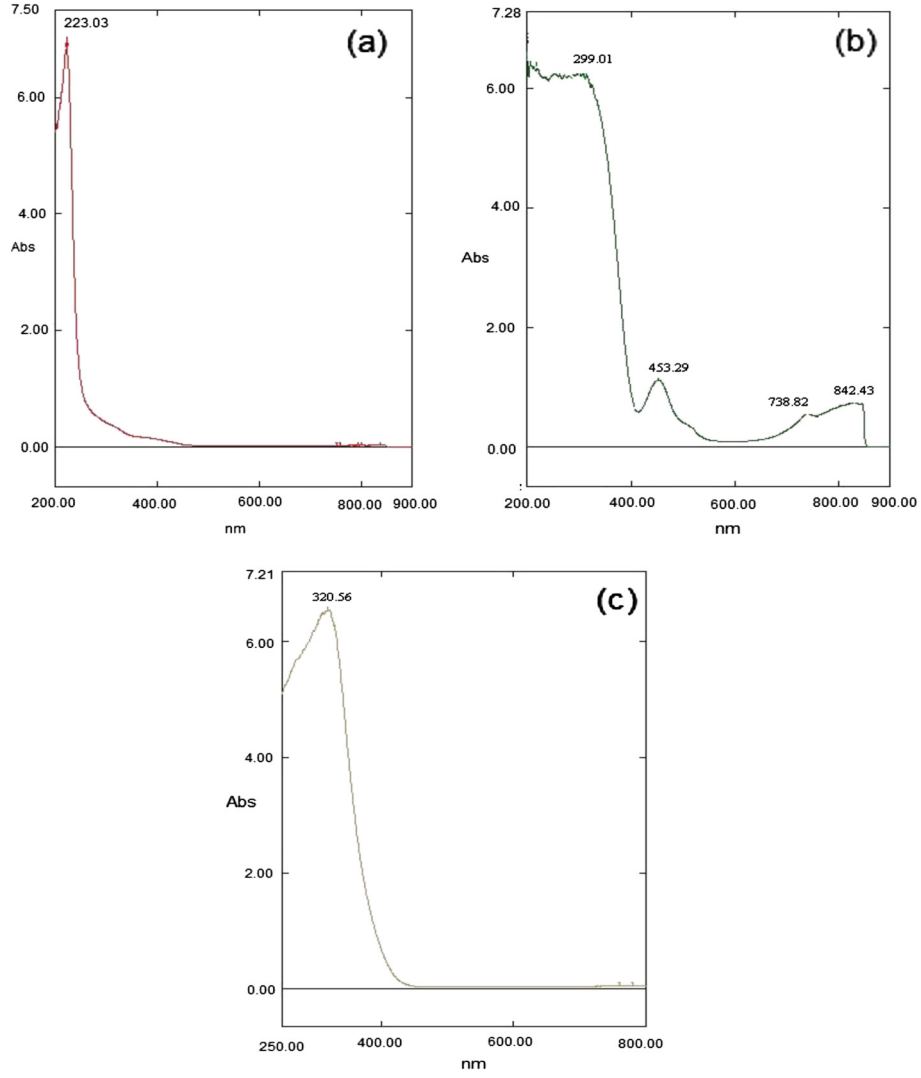

Figure 5 Optical absorbance spectra of the metal tungstates. (**a**) $BaWO_4$, (**b**) $NiWO_4$ and (**c**) Bi_2WO_6.

(2.97 eV), 453 nm (2.71 eV), 738 nm (1.68 eV) and 842 nm (1.47 eV) are observed; the first and second bands with high intensity are in the ultraviolet range while the third and forth with low intensity is in the blue range. The first band at 2.97 eV may be attributed to the charge transfer transition in the WO_6 matrix. Bands at 2.71 and 1.68 eV are assigned to the forbidden electronic transition from $^3A_{2g}$ to ^1E_g and $^1T_{2g}$, respectively. The band at 1.47 eV can be assigned to the presence of $Ni^{2+}O_4$ arising from Frenkel defects with dislocation of Ni^{2+} from the octahedral to tetrahedral sites. This result is in agreement with that of de Oliveira et al. [37].

Quantification of the band gap (E_g) was carried out for all three metal tungstate samples. The band gap transition is determined from the steep shape of the spectra and the equation $\alpha h\nu = A(h\nu - E_g)^m$ was employed where the absorption coefficient (α) is related to the incident photon energy ($h\nu$), A is constant, m is the index indicating the type of transition [38]. The nature of the electropositive ions (Ba^{2+}, Ni^{2+} and Bi^{3+}) seems to have small influence on the E_g values. It is found that E_g decreases according to the following sequence: $BaWO_4$ > Bi_2WO_6 > $NiWO_4$ (Table 3). The band gap of $BaWO_4$ (4.60 eV) agrees well with the values reported [39,40], while the value of the prepared $NiWO_4$ is significantly higher (3.05 eV) [41,42]. Ross-Medgaarden and Wachs [14] also reported the E_g value of wolframite $NiWO_4$ as ~4.5 eV, which is higher than this finding with ligand-to -metal charge transfer (LCMT) band maximum between 247-252 and 342-344 nm, due to the distortion nature in isolated WO_6 units.

For Bi_2WO_6, the band gap value obtained (3.05 eV) is higher than that found by Fu et al. [43], as the E_g value in d° perovskites was shown to depend upon the electro-

Table 3 Summary of metal tungstates wavelength and band gap energy

System	Wavelength (nm)	Eg (eV) this work	Eg (eV) literature	Ionic radius of cation A (Å)
Bi_2WO_6	320.56	3.05	2.7 [43]	2.67
$BaWO_4$	223.03	4.60	4.8- 5.58 [39,40]	1.42
$NiWO_4$	299.03	2.97	2.28- 2.95 [41,42] 4.5 [14]	0.69

negativity of the transition metal ion, the connectivity of the polyhedral and the deviation from linearity of the M-O-M bonds. In addition, the forms of the solid samples often have strong effect on the optical properties of the material [22].

PL spectra

Figure 6 shows the PL spectra of $BaWO_4$, Bi_2WO_6 and $NiWO_4$ using the excited wavelength of 325 nm. Broad blue-green emission peaks centered at ~600 nm are observed. This profile of the emission band is typical of a multiphonon process, i.e., a system in which relaxation occurs by various paths, involving the participation of numerous states. The emission peaks are attributed to the recombination of electrons in the $^1T_2$ excited state and holes in the $^1A_1$ ground state, specified within the $[WO_4]^{2-}$ excited complexes. The blue component is attributed to the regular lattice of which the emitting level comprises both metal cations (Ba, Ni and Bi) and tungstate contributions, while the green one originates from the defect centers associated with oxygen [44]. Meanwhile the broad peaks are due to the transition from the $^3T_1$ and $^3T_2$ excited states to the $^1A_1$ ground state [24].

It has been reported that metal tungstates exhibit blue luminescence spectra, which is based on the radiative transition within the tetrahedral (WO_4^{2-}) group [45]. From Table 4, $BaWO_4$ nanoparticles exhibit higher emission intensity than the other two samples (Bi_2WO_6 and $NiWO_4$). The PL intensity is controlled by the number of charged transfers and surface defects. Moreover, the emission peaks obviously shift to the region of long wavelength which may be due to the particle-forming effect and the increased size of nanoparticles [46,47].

For Bi_2WO_6, smaller grain size also contributes considerably to high PL intensity. Similar observations were also observed by Dong Young et al. who synthesized Bi_2WO_6 hydrothermally and obtained higher PL intensity with the smaller crystallite size of 23 nm as calculated from XRD [48]. These phenomenon closely agrees to that reported by Quintana-Melgoza et al. [25] in which the optical response of material is largely determined by its underlying electronic properties that are closely related to its chemical or ions, atomic arrangement and physical dimension for nanometer-sized materials. Low intensity of the PL curve has been shown to be due to the oxygen atoms playing the role of electron capturers, thereby depressing the recombination process. In addition, PL intensity also depends on whether the added tungsten metal acts as an electron capturer or not. The PL curve of $NiWO_4$ powder tends to shift slightly to a higher wavelength as compared to Bi_2WO_6 and $BaWO_4$. This blue shift is observed when the dimensions of nanocrystalline particles approach the

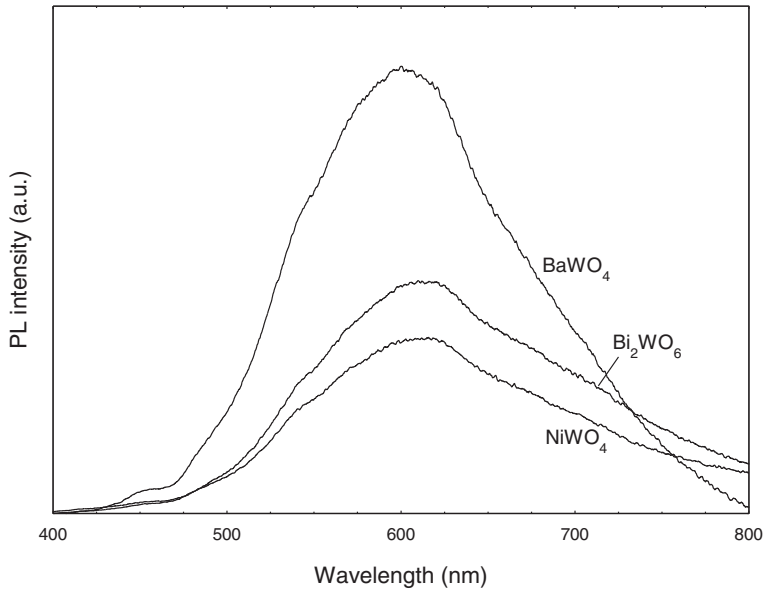

Figure 6 Photoluminescence spectra of $BaWO_4$, $NiWO_4$ and Bi_2WO_6 samples.

Table 4 Summary of wavelength at maximum peak and peak intensity of $BaWO_4$, $NiWO_4$ and Bi_2WO_6 samples

System	Intensity (a.u.)	Wavelength (nm)
$NiWO_4$	921	615
$BaWO_4$	2600	603
Bi_2WO_6	1215	610

exciton Bohr radius (a_o) due to the quantum-size effect (quantum confinement phenomenon) which can be attributed to the wider band gap [49] thus agreeing with the finding on band gap calculation in Table 3. Lee et al. [49] on discussing the effective mass model has assumed that blue shift in the band gap energy occurs due to spatial confinement of an exciton. Hence to generate a free exciton, energy higher than the effective band gap energy must be available. In the absence of additional levels introduced by defects, radiative electron-hole recombination of this free exciton should result in photon emission with energy equivalent to the band gap energy. Although there are different opinions explaining the origin of the emission bands and the nature of the optical transition is unclear, the WO_4^{2-} complex and the slight deviation from a perfect crystal structure are believed to be responsible for the emission bands.

Conclusions

Three different phases of metal tungstates of $BaWO_4$ (scheelite), $NiWO_4$ (wolframite) and Bi_2WO_6 (perovskite layer) were successfully prepared by the simple and economical sucrose-templated method. The highest surface area (20.06 m^2g^{-1}) contributed by of $NiWO_4$ is believed to arise from higher pore distribution and less particle agglomeration due to the presence of sucrose. Raman spectra showed that the vibration modes of the products are in accordance to those of the tungstate compounds. Microstructure vibrations of three different phases of scheelite-type $BaWO_4$ were shown to have less Raman active modes when compared to wolframite $NiWO_4$, caused from the increased lattice symmetry while layered perovskite Bi_2WO_6 exhibited only four peaks involving oxygen motion, perpendicular and within the layer. Slight shifting of the detected vibration modes and that some vibration modes were not detected can be attributed to some differences in their geometries, particle sizes and nature of the products. The UV spectra revealed the highest band gap associated with $BaWO_4$ followed by Bi_2WO_6 and $NiWO_4$. Broad blue-green emission peaks in PL were detected at ~ 600 nm for all samples. The blue-shift in PL spectra is due to the quantum size effect as a result of the wider band gap. Results also showed great dependence of the PL intensity on smaller grain sizes (~ 50-80 nm) with homogenous spherical particle morphology. The materials showed promising PL results for fluorescence lamp application.

Competing interests

The authors declare that they have no competing interests.

Authors' contribution

SMMZ carried out the experimental work, RY, AH, HNMEM and MND participating in the interpretation and discussion of the results. All authors read and approved the final manuscript.

Acknowledgement

The authors gratefully acknowledged the financial support granted by the Ministry of Higher Education, Malaysia (FRGS: FP056/2008C) and University of Malaya (PPP: PV035/2011B).

Received: 29 January 2013 Accepted: 16 April 2013
Published: 1 May 2013

References

1. Wang BG, Shi EW, Zhong WZ, Yin ZW: **Relationship between the orientations of tetrahedral $[WO_4]^{2-}$ in tungstate crystals and their morphology.** *J Inorg Mater* 1998, **13:**648–654.
2. Koepke C, Wojtowicz AJ, Lempicki A: **Excited-state absorption in excimer-pumped $CaWO_4$, crystals.** *J Luminescence* 1993, **54:**345–355.
3. Sinelnikov BM, Sokolenko EV, Zvekov VY: **The Nature of Green Luminescence Centers in Scheelite.** *Inorg Mater* 1996, **32:**999–1001.
4. Cooper TG, Leeuw NH: **A combined ab initio and atomistic simulation study of the surface and interfacial structures and energies of hydrated scheelite: Introducing a $CaWO_4$ potential model.** *Surf Sci* 2003, **531:**159–179.
5. Cho W, Yashima M, Kakihana M, Kudo A, Sakata T, Yoshimura M: **Room--temperature preparation of the highly crystallized luminescent $CaWO_4$ film by an electrochemical method.** *Appl Phys Lett* 1995, **66:**1027–1029.
6. Kuzmin A, Purans J: **Local atomic and electronic structure of tungsten ions in AWO_4 crystals of scheelite and wolframite types.** *Rad. Meas.* 2001, **33:**583–586.
7. Grobelna B, Lipowska B, Klonkowski AM: **Energy transfer in calcium tungstate doped with Eu(III) or Tb(III) ions incorporated into silica xerogel.** *J Alloys Compd* 2006, **419:**191–196.
8. Tamaki J, Fujii T, Fujimori K, Miura N, Yamazoe N: **Application of metal tungstate-carbonate composite to nitrogen oxides sensor operative at elevated temperature.** *Sensors and Actuators B* 1995, **24**(5):396–399.
9. Stern DL, Grasselli RK: **Propane oxydehydrogenation over metal tungstates.** *J Catal* 1997, **167**(2):570–572.
10. Yu SH, Liu B, Mo MS, Huang JH, Li XM, Qian YT: **General synthesis of single crystal tungstate nanorods/nanowires: A facile low temperature solution approach.** *Adv Funct Mater* 2002, **13**(8):639–647.
11. Hongbo F, Shaogui Y, Shicheng Z, Zhijian Z: **Preparation of nanosized Bi2WO6 using different content of starting materials and their photoactivities.** *J Appl Spectrosc* 2009, **76**(2):227–233.
12. Lacomba-Perales R, Errandonea D, Martinez-Garcia D, Hern□ ndez R, Radescu S, Mujica A, Muñoz A, Chervin JC, Polian A: **Phase transitions in wolframite-type $CdWO_4$ at high pressure studied by Raman spectroscopy and density-functional theory.** *Physical Revision B* 2009, **79:**94105–94115.
13. Cavalcante LS, Sczancoski JC, LF Lima JR, Espinosa JWM, Pizani PS: **Synthesis, Characterization, Anisotropic Growth and Photoluminescence of $BaWO_4$ Crystal.** *Growth & Design* 2009, **9**(2):1002–1012.
14. Ross-Medgaarden EI, Wachs IE: **Structural Determination of Bulk and Surface Tungsten Oxides with UV–vis Diffuse Reflectance Spectroscopy and Raman Spectroscopy.** *J Phys Chem C* 2007, **111:**15089–15099.
15. Siriwong P, Thongtem T, Phuruangrat A, Thongtem S: **Hydrothermal synthesis, characterization, and optical properties of wolframite $ZnWO_4$ nanorods.** *Cryst Eng Comm* 2011, **13:**1564–1569.
16. Shi S, Liu X, Gao J, Zhou J: **Spectroscopic properties and intense red-light emission of (Ca, Eu, M)WO_4 (M = Mg, Zn, Li).** *Spectrochimica Acta Part A* 2008, **69:**396–399.
17. Huang JY, Jia QX: **Structural properties of $SrWO_4$ films synthesized by pulsed-laser deposition.** *Thin Solid Films* 2003, **444:**95–98.

18. Dong Young K, Sujung K, Misook K: **Synthesis of Bi_2WO_6 Nanometer Sheet Shaped and Approach to the Photocatalysis, Bull.** *Korean Chem Soc* 2009, **30**(3):630–635.
19. Afanasiev P: **Molten salt synthesis of barium molybdate and tungstate microcrystals.** *Material Letters* 2007, **61:**4622–4626.
20. Song Z, Ma J, Sun H, Wang W, Sun Y, Sun L, Liu Z, Gao C: **Synthesis of $NiWO_4$ nano-particles in low-temperature molten salt medium.** *Ceram Int* 2009, **35:**2675–2678.
21. Prabhakaran K, Melkeri A, Gokhale NM, Sharma SC: **Synthesis of nanocrystalline 8 mol% yttria stabilized zirconia powder from sucrose derived organic precursors.** *Ceram Int* 2007, **33:**1551–1555.
22. Yujie W, Bandyopadhyay A, Bose S: **Processing of alumina and zirconia nano-powders and compacts.** *Mat Science Eng* 2004, **380:**349–355.
23. Ruiz-Fertes J, López-Moreno S, Segura A, Rodríguez-Hernandez P, Munoz A, Romero AH, Gonzales J: **High-pressure phase transitions and compressibility of wolframite-type tungstates.** *J Appl Phys* 2010, **107:**083506–10.
24. Anukorn P, Titipun T, Somchai T: **Barium molybdate and barium tungstate nanocrystals synthesized by a cyclic microwave irradiation.** *J Phys Chem Solids* 2009, **70**(6):955–959.
25. Quintana-Melgoza JM, Cruz-Reyes J, Avalos-Borja M: **Synthesis and characterization of $NiWO_4$ crystals.** *Material Letters* 2001, **47:**317–318.
26. Thangadurai V, Knittlmayer C, Weppner W: **Metathetic room temperature preparation and characterization of scheelite-type ABO_4 (A = Ca, Sr, Ba, Pb; B = Mo, W) powders.** *Mat Science Eng* 2004, **106:**228–233.
27. Quintana-Melgoza JM, Gomez-Cortes A, Avalos-Borja M: **Reduction of NO by CO over NiWO4, NiO and WO3 catalysts.** *React Kinet Catal Lett* 2002, **76**(1):131–140.
28. Alfaro SO, Martínez-de la Cruz A: **Synthesis, characterization and visible-light photocatalytic properties of Bi_2WO_6 and $Bi_2W_2O_9$ obtained by co-precipitation method.** *Appl Catal Gen A* 2010, **383:**128–133.
29. Cavalcante LS, Sczancoski JC, Lima LF Jr, Espinosa JWM, Pizani PS, Varela JA, Longo E: **Synthesis, Characterization, Anisotropic Growth and Photoluminescence of BaWO4.** *Crystal Growth Design* 2009, **9**(2):1002–1012.
30. Hardcastle FD, Wachs IE: **Determination of the molecular structures of tungstates by Raman spectroscopy.** *J Raman Spectrosc* 1995, **26**(6):397–405.
31. Hoffart L, Heider U, Jörissen J, Huggins RA, Witschel W: **Transport properties of materials with the scheelite structure.** *Solid State Ionics* 1994, **72:**195–198.
32. Basiev TT, Sobol AA, Voronko YK, Zverev PG: **Spontaneous Raman spectroscopy of tungstate and molybdate crystals for Raman lasers.** *Optical Material* 2000, **15:**205–216.
33. Rondinone AJ, Pawel M, Travaglini D, Mahurin S, Dai S: **Metastable tetragonal phase $CdWO_4$ nanoparticles synthesized with a solvothermal method.** *J Colloid Interface Sci* 2007, **306:**281–284.
34. Jayaraman SY, Wang SK: **Sharma, High-pressure Raman investigation on $CdMoO_4$ and pressure-induced phase transformations.** *Physic Revision B* 1995, **52:**9886–9889.
35. Blasse G: **Vibrational spectra of $HgMoO_4$ and $HgWO_4$.** *Inorganic J Nuclear Chem* 1975, **37:**97–99.
36. Frost RL, Duong L, Weiver M: **Raman microscopy of selected tungstate minerals.** *Spectrochimica Acta Part A Mol Biomol Spectroscopy* 2004, **60:**1853–1859.
37. de Oliveira JMFALM, Silva MRS, de Souza SC, Vieira FTG, Longo E, Souza AG, Leda MG S: **Influence of the thermal treatment in the crystallization of $NiWO_4$ and $ZnWO_4$.** *J Thermal Anal Calorim* 2009, **97:**167–172.
38. Alessandro Cimino M, Lo J, Schiavello M: **Structural, magnetic, and optical properties of nickel oxide supported on βeta.- and γgamma.-aluminas.** *J Phys Chem* 1971, **75:**1044–1050.
39. Lenglet M, H F, Durr J, Tuilier MH: **Investigation of the chemical bonding in $3d^8$ nickel(II) charge transfer insulators (NiO, oxidic spinels) from ligand-field spectroscopy, Ni 2*p* XPS and X-ray absorption spectroscopy.** *Solid State Commun* 1997, **104:**793–798.
40. Pontes FM, Maurera MAMA, Souza AG, Longo E, Leite ER, Magnani R, Machado MAC, Pizani PS, Varela JA: **Preparation, structural and optical characterization of $BaWO_4$ and $PbWO_4$ thin films prepared by a chemical route.** *J Eur Ceram Soc* 2003, **23:**3001–3007.
41. Purnendu P, Karthik TN, Manivannan V: **Synthesis and characterization of metal tungstates by novel solid-state metathetic approach.** *J Alloys Compd* 2008, **6:**380–386.
42. Tiziano Montini VG, Abdul H, Laura F, Gianpiero A, Paolo F: **Synthesis, characterization and photocatalytic performance of transition metal tungstates.** *Chem Phys Lett* 2010, **498:**115–116.
43. Fu H, Pan C, Yao W, Zhu Y: **Visible-light-induced degradation of Rhodamine B by nanosized Bi2WO6.** *J Phys Chem B* 2005, **190:**22432–22439.
44. Prashant Kumar P, Bhave NS, Kharat RB: **Structural, optical, electrical and photovoltaic electrochemical characterization of spray deposited $NiWO_4$ thin films.** *Electrochim Acta* 2006, **51:**4659–4664.
45. Blasse G: **Classical phosphors: A Pandora's box.** *J Luminescence* 1997, **72–74:**129–134.
46. Thresiamma G, Sunny J, Sunny AT, Suresh M: **Fascinating morphologies of lead tungstate nanostructures by chimie douce approach.** *J Nanopart Res* 2008, **10:**567–575.
47. Shen Y, Li W, Li T: **Microwave-assisted synthesis of BaWO4 nanoparticles and its photoluminescence properties.** *Mater Lett* 2011, **65:**2956–2958.
48. Dong Young K, Sujung K, Misook K: **Synthesis of Bi2WO6 Nanometer Sheet Shaped and Approach to the Photocatalysis.** *Bull Korean Chem Soc* 2009, **30**(3):630–635.
49. Lee EJH, Ribeiro C, Giraldi TR, Longo E, Leite ER: **Photoluminescence in quantum-confined SnO2 nanocrystal: Evidence of free exciton decay.** *Applied Physics Letters* 2004, **84:**1745–1747.

doi:10.1186/1752-153X-7-80
Cite this article as: M Zawawi *et al.*: Structural and optical characterization of metal tungstates (MWO_4; M=Ni, Ba, Bi) synthesized by a sucrose-templated method. *Chemistry Central Journal* 2013 **7**:80.